

Dipendra Kumar Roy¹, Rajiv Tiwari²

Development of identification procedure for the internal and external damping in a cracked rotor system undergoing forward and backward whirls

In the present work, a procedure for the estimation of internal damping in a cracked rotor system is described. The internal (or rotating) damping is one of the important rotor system parameters and it contributes to the instability of the system above its critical speed. A rotor with a crack during fatigue loading has rubbing action between the two crack faces, which contributes to the internal damping. Hence, internal damping estimation also can be an indicator of the presence of a crack. A cracked rotor system with an offset disc, which incorporates the rotary and translatory of inertia and gyroscopic effect of the disc is considered. The transverse crack is modeled based on the switching crack assumption, which gives multiple harmonics excitation to the rotor system. Moreover, due to the crack asymmetry, the multiple harmonic excitations leads to the forward and backward whirls in the rotor orbit. Based on equations of motions derived in the frequency domain (full spectrum), an estimation procedure is evolved to identify the internal and external damping, the additive crack stiffness and unbalance in the rotor system. Numerically, the identification procedure is tested using noisy responses and bias errors in system parameters.

1. Introduction

In industry, high-speed rotating machinery requires the operation in a stable speed region to evade premature failure of components and to ensure the personnel safety. Hence, the prediction of the instability at the design stage itself of such a

✉ R. Tiwari, e-mail: rtiwari@iitg.ac.in

¹Department of Mechanical Engineering, Indian Institute of Technology Guwahati, Guwahati, Assam, 781039, India. E-mail: r.dipendra@iitg.ac.in

²Faculty of Mechanical Engineering, Indian Institute of Technology Guwahati, Guwahati, Assam, 781039, India.



machinery is very crucial. However, it requires accurate modeling and analysis of physical phenomena leading to instability. One of the many causes of the rotor instability is the existence of internal (or rotating) damping. This type of damping occurs owing to rubbing of free surfaces (shaft-disc interfaces, crack free faces, etc.) and/or the material hysteresis during the shaft rotation. Theoretical procedures to accurately estimate the internal damping of intact shaft in available damping mathematical models are quite challenging in rotor systems [1]. Moreover, it is to emphasize that the internal damping could also come from the crack and, from this aspect, hardly any literature is available. The analysis on the micro-rubbing of surfaces in mechanical parts and joints and its effect on dynamics of bigger structures (the so-called structural friction) are available but these are non-rotating structures.

Very few attempts have been made on the internal damping identification. However, in literature, the instability analysis due to the internal damping has been dealt with in detail. Ehrich [2] studied the spin speed stability regions with different whirl modes for different internal damping condition. Shaw and Shaw [3] elaborated the stable and unstable regions of the whirl mode in a rotor system based on the ratio of external and internal damping with increasing spin speed. Kurnik [4] analyzed the stability of rotating shaft with the internal and external damping with speed variation from the subcritical to supercritical speeds. Chen and Ku [5] and Ku [6] worked on analysis of the forward and backward whirls in the region of stability owing to the effect of the internal and hysteretic damping. The rotary and translational inertia are considered including the gyroscopic couple in a rotor-bearing system based on the Timoshenko beam theory. Melanson and Zu [7], based on the Timoshenko beam model, studied the stability of rotating machinery, considering the external damping and hysteretic damping. Genta [8] discussed the effect of hysteretic damping at the critical, subcritical and supercritical speeds for a rotor system in the forward and backward whirling motions. Dynamic instability of the rotor system was also studied by Dimentberg [9] and Vatta and Vigliani [10] due to random variations of the system internal damping. The stability analysis of viscous internal damping and dry friction damping at rotor-shaft joints was considered in a rotor system by Fischer and Strackeljan [11]. Using the Euler–Bernoulli beam theory in rotor system by considering the effect of rotary and translational inertia with a gyroscopic moment of the disc, the external and hysteretic damping was estimated by Montagnier and Hochard [12]. Chouksey et al. [13] worked on the modal analysis to study the effect of the internal damping influence of the shaft and fluid film forces (external damping) from journal bearings on the rotor system instability. The effect of the shaft material (internal) damping is found to reduce the stability limit speed.

Full-spectrum based regression methods have been used by many authors for different fault identification. For example, in the identification of fault parameters of rotating machinery, i.e., the residual unbalance, crack, viscous (external) damping, etc. The feature-based identification of malfunctioning of rotating machinery based

on full-spectrum in the forward and backward whirling was proposed by Goldman and Muszynska [14]. The full-spectrum conveys the sense of rotation of a particular whirl orbit in the forward or backward direction with respect to the spinning direction of the rotor. Tiwari [15] presented a detail discussion on the identification of the residual unbalance and bearing dynamic parameters in a multi-degrees-of-freedom rotor-bearing system based on the regression method.

Several researchers have worked on the crack identification including other system parameters, like external damping, unbalance, misalignment, etc. Mayes and Davies [16] described the transverse crack opening and closure in the rotor shaft based on vibration in a rotor-bearing system. Gasch [17] illustrated the dynamic response of a Laval rotor in the presence of transverse crack and unbalance. Karthikeyan et al. [18], and Singh and Tiwari [19] used the finite element modeling and developed algorithms to estimate the size and location of cracks in a shaft system. Shrivankumar and Tiwari [20], and Sandeep Singh and Tiwari [21] worked on a transverse cracked shaft to identify different system parameters, such as the additive crack stiffness, viscous damping, and disc eccentricity. They assumed the crack model as the switching crack, and the full spectrum in multi-harmonics was used for the identification of the parameters based on the regression matrix method. Sandeep Singh and Tiwari [22, 23] extended the identification of crack parameters in a Jeffcott rotor active magnetic bearing model with an offset disc considering gyroscopic effect.

It is clear from the literature review that research works so far focused on the estimation of internal damping or estimation of crack parameters along with the other rotor system parameters. However, limited or no work has been reported on the combined effect of coexistence of crack and associated internal damping, which is very much of practical importance. This is because the internal damping estimation can give an indication of crack growth in rotors. Therefore, in the current work, estimation of the internal damping owing to the rotor crack effect is being attempted. The system model has a simple rotor with an offset disc and an assumption of switching crack has been made to mathematically model the crack function. The offset disc gives rise to the gyroscopic effect, and based on these considerations the equations of motion (EOMs) are derived. The dynamic condensation has been applied to eliminate two rotational (due to tilting of the disc) displacements from the EOMs, which are difficult to measure in practice. The full spectrum of responses is obtained by two methods, the first method is based on the regression method and the second method is based on the fast Fourier transform (FFT). However, the FFT-based full spectrum needs a phase correction with respect to a reference signal. Based on EOMs in frequency domain, an identification procedure has been developed, which estimates the internal damping and other crucial system unknown parameters, like the external damping, unbalance and crack stiffness. The effectiveness of the present model-based identification procedure has been tested numerically against different noise levels in responses and bias errors in system parameters.

2. System model

This section presents the derivation of EOMs of a cracked rotor. The rotor consists of a crack shaft incorporating the internal damping due to crack and the gyroscopic effect owing to the offset disc. Moreover, it includes the external damping and unbalance. The generation of numerical responses in full spectrum has been also been described.

2.1. Configuration of rotor model and equations of motion

In this work, a simple rotor model configuration is considered with a transverse crack near the offset disc, as shown in Fig. 1. The support bearings at both the ends are assumed to be transversely rigid, which allows the rotations of the shaft. Point O is the origin on the bearing axis line and near the disc, z is the bearing axis and x is the vertical axis in the downward direction (along the direction of gravity). Let mg be the weight of the disc, φ_{y0} represent the initial (static) tilting of disc and u_{x0} is the static deflection of the disc. Rotational coordinate axes are ξ and η . The crack front direction is considered in the ξ axis. Disc translation displacements are shown in Fig. 2. Let ω be the shaft spin speed and t represents the time. Points C and G represent the geometric center and center of gravity of the disc, respectively.

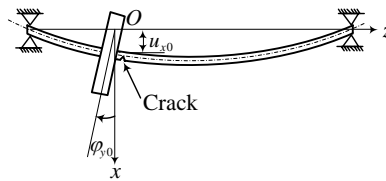


Fig. 1. Jeffcott rotor with an offset disc in the presence of a transverse crack in static condition

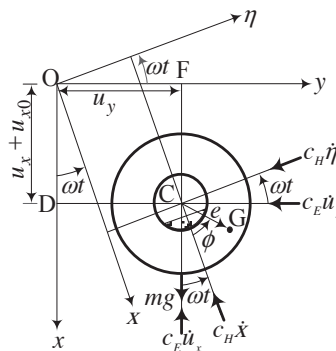


Fig. 2. The rotor with unbalance, self-weight, internal and external damping force and displacement ($x = u_x + u_{x0}$ and $y = u_y$) with respect to the fixed and rotating frame of references

Let e be the radial eccentricity of the disc, which is the distance between C and G, and ϕ is the phase angle between the unbalance force and the crack front direction (i.e., ξ axis direction). Forces due the internal damping (c_H), external damping (c_E) and the gravity are shown in Fig. 2.

EOMs of the rotor with the cracked shaft and offset disc considering of gyroscopic effects, however, without internal damping are given as ([24])

$$\mathbf{M}\ddot{\mathbf{q}}(t) + (\mathbf{C}_E - \omega\mathbf{G})\dot{\mathbf{q}}(t) + (\mathbf{K} - \Delta\mathbf{K}(u, t))\mathbf{q}(t) = \mathbf{f}_{st} + \mathbf{f}_{umb}(t). \quad (1)$$

Here \mathbf{M} , \mathbf{C}_E , \mathbf{G} , and \mathbf{K} are the mass matrix, external damping matrix, gyroscopic matrix, and stiffness matrix, respectively. In addition, the matrix $\Delta\mathbf{K}$ is the flexibility matrix owing to the crack and details of it are discussed in the next section. Vectors \mathbf{f}_{st} and \mathbf{f}_{umb} are force vectors owing to the static deflection and the unbalance, respectively; \mathbf{q} is the vector of displacement, and $\dot{\mathbf{q}}$ and $\ddot{\mathbf{q}}$ are the first and second time derivatives of \mathbf{q} . Various matrices and vectors are given in Appendix A (Equation (A1)).

2.2. Internal damping model

The internal damping comes on the shaft owing to the rubbing of two faces of a crack, rubbing between disc and shaft, and due to hysteresis. Let the combined form of internal viscous damping factor be c_H . Forces due this are shown in Fig. 2 along with external viscous damping force. These forces in the stationary coordinate system can be written as

$$f_{xd}(t) = c_H\dot{\xi} \cos(\omega t) - c_H\dot{\eta} \sin(\omega t) + c_E\dot{u}_x \quad (2)$$

and

$$f_{yd}(t) = c_H\dot{\xi} \sin(\omega t) + c_H\dot{\eta} \cos(\omega t) + c_E\dot{u}_y. \quad (3)$$

On combining damping forces in the complex form, we get

$$f_{cd}(t) = f_{xd}(t) + jf_{yd}(t). \quad (4)$$

On using Equations (2) and (3) in Equation (4), we get

$$f_{cd}(t) = c_H\dot{\zeta}e^{j\omega t} + c_E\dot{r}. \quad (5)$$

Defining $\zeta = \xi + j\eta$ one gets the complex displacement in a rotating coordinate system with $j = \sqrt{-1}$, and $r = x + jy$ is the complex displacement in the stationary coordinate system. This gives $\dot{\zeta} = \dot{\xi} + j\dot{\eta}$ and $\dot{r} = \dot{x} + j\dot{y}$ as the derivatives of complex displacement. The transformation from the stationary coordinate system to the rotating coordinate system is given as $\zeta = re^{-j\omega t}$ with $\dot{\zeta} = (\dot{r} - j\omega r)e^{-j\omega t}$. Hence, the damping force takes in the following form

$$f_{cd}(t) = c_H(\dot{r} - j\omega r) + c_E\dot{r}. \quad (6)$$

The details of the matrices and vectors are given in Appendix A (Equations (A2)). On including the internal damping, the system of Equation (1) takes the following form

$$\mathbf{M}\ddot{\mathbf{q}} + (\mathbf{C}_E + \mathbf{C}_H - \omega\mathbf{G})\dot{\mathbf{q}} + (\omega\mathbf{C}_{1H} + \mathbf{K} - \Delta\mathbf{K}(s, t))\mathbf{q} = \mathbf{f}_{st} + \mathbf{f}_{unb}(t). \quad (7)$$

The detail of the matrices is given in Appendix A (Equations (A3)). We have $\mathbf{q}(t) = \mathbf{q}_v(t) + \mathbf{q}_0$, so that $\dot{\mathbf{q}}(t) = \dot{\mathbf{q}}_v(t)$ and $\ddot{\mathbf{q}}(t) = \ddot{\mathbf{q}}_v(t)$. Equation (7) takes the following form

$$\begin{aligned} \mathbf{M}\ddot{\mathbf{q}}_v + (\mathbf{C}_E + \mathbf{C}_H - \omega\mathbf{G})\dot{\mathbf{q}}_v + (\omega\mathbf{C}_{1H} + \mathbf{K})\mathbf{q}_v \\ = \Delta\mathbf{K}(s, t)(\mathbf{q}_v + \mathbf{q}_0) - \omega\mathbf{C}_{1H}\mathbf{q}_0 + \mathbf{f}_{unb}(t) \end{aligned} \quad (8)$$

with $\mathbf{K}\mathbf{q}_0 = \mathbf{f}_{st}$, for the static condition, and details of the solution of \mathbf{q}_0 are given in appendix Equations (A4) to (A5). Based on the weight dominance, in Equation (8), the terms $\mathbf{q}_v(t)$ in right-hand side can be ignored as compared to the static deflection, \mathbf{q}_0 , because of \mathbf{q}_0 is much larger than $\mathbf{q}_v(t)$ owing to the heavy weight of the rotor ([22]). Hence, the modified EOM is

$$\begin{aligned} \mathbf{M}\ddot{\mathbf{q}}_v + (\mathbf{C}_E + \mathbf{C}_H - \omega\mathbf{G})\dot{\mathbf{q}}_v + (\omega\mathbf{C}_{1H} + \mathbf{K})\mathbf{q}_v \\ = \Delta\mathbf{K}(s, t)\mathbf{q}_0 - \omega\mathbf{C}_{1H}\mathbf{q}_0 + \mathbf{f}_{unb}(t). \end{aligned} \quad (9)$$

2.3. Model of the Crack

The load (forces and moments) direction based on a transverse crack representation is shown in Fig. 3. The additional flexibility matrix because of the crack, on the basis of the fracture mechanics approach, is generally used as a crack model [22, 25]. The time-dependent additive crack has the following form

$$\Delta\mathbf{K}'_{rot}(t) = \sigma(t)\Delta\mathbf{K}'_{rot}. \quad (10)$$

The shaft stiffness in the closed condition of the crack is \mathbf{K}'_{rot} (which is the same as the intact shaft stiffness) and for the crack open condition is $\mathbf{K}'_{rot} - \Delta\mathbf{K}'_{rot}$. Here,

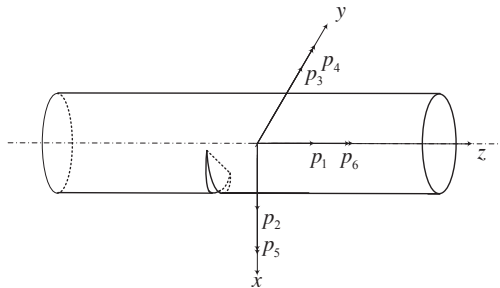


Fig. 3. Various load directions across the transverse crack in a rotor element

$\Delta\mathbf{K}'_{rot}$ is the additive crack stiffness, which comes into picture when the crack is in open condition. In the rotating shaft, $\Delta\mathbf{K}'_{rot}$ is not considered when the crack is in the closed condition and is subtracted only in its open condition. Thus, it represents a switch on-off mode of the crack, which is a time-dependent phenomenon. To model this behavior, a switching crack model of an additive stiffness excitation function is chosen based on the Fourier-series [17]. It considers a switching crack excitation function (SCEF) as $\sigma(t)$. The general SCEF for a rectangular function is given as,

$$\sigma(t) = \frac{1}{2} + \frac{2}{\pi} \cos(\omega t) - \frac{2}{3\pi} \cos(3\omega t) + \frac{2}{5\pi} \cos(5\omega t) - \frac{2}{7\pi} \cos(7\omega t) + \dots \quad (11)$$

The stiffness matrix of the intact shaft, the crack stiffness matrix and the force vector is expressed in the static frame of reference, as

$$\begin{aligned} \mathbf{K}' &= \mathbf{T}^T \mathbf{K}'_{rot} \mathbf{T}, \\ \Delta\mathbf{K}'(t) &= \mathbf{T}^T \Delta\mathbf{K}'_{rot} \mathbf{T}, \\ \mathbf{f}_{cr}(t) &= \sigma(t) \Delta\mathbf{K}'(t) \mathbf{q}_0, \end{aligned} \quad (12)$$

which can be written in the expanded form, as

$$\mathbf{f}_{cr}(t) = \frac{1}{2} \sigma(t) \begin{Bmatrix} \Delta k_{22}(1 + \cos 2\omega t) u_{x0} \\ \Delta k_{22} \sin(2\omega t) u_{x0} \\ \Delta k_{44}(1 + \cos 2\omega t) \varphi_{y0} \\ \Delta k_{44} \sin(2\omega t) \varphi_{y0} \end{Bmatrix}. \quad (13)$$

Noting Equations (9) and (13), the EOM takes the following form

$$\mathbf{M}\ddot{\mathbf{q}}_v + (\mathbf{C}_E + \mathbf{C}_H - \omega\mathbf{G}) \dot{\mathbf{q}}_v + (\omega\mathbf{C}_{1H} + \mathbf{K}) \mathbf{q}_v = \mathbf{f}_{cr}(t) - \omega\mathbf{C}_{1H}\mathbf{q}_0 + \mathbf{f}_{umb}(t). \quad (14)$$

Equation (14) in the complex form can be expressed, as

$$\overline{\mathbf{M}}\ddot{\mathbf{v}} + (\overline{\mathbf{C}}_E + \overline{\mathbf{C}}_H - j\omega\overline{\mathbf{G}}) \dot{\mathbf{v}} + (\overline{\mathbf{K}} - j\omega\overline{\mathbf{C}}_H) \mathbf{v} = \overline{\mathbf{f}}_{cr}(t) + \overline{\mathbf{f}}_{umb}(t) + j\omega\mathbf{C}_H \begin{Bmatrix} u_{x0} \\ 0 \end{Bmatrix} \quad (15)$$

with

$$r = u_x + ju_y, \quad \varphi = \varphi_y + j\varphi_x,$$

$$(-I_p\omega\dot{\varphi}_x) + j(I_p\omega\dot{\varphi}_y) = jI_p\omega\dot{\varphi}, \quad \omega\mathbf{C}_H u_y - j\omega\mathbf{C}_H u_x = -j\omega\mathbf{C}_H r, \quad u_{x0} + ju_{y0} = r_0 e^{j\theta}$$

$$\begin{aligned} \overline{\mathbf{M}} &= \begin{bmatrix} m & 0 \\ 0 & I_d \end{bmatrix}, & \overline{\mathbf{C}}_E &= \begin{bmatrix} c_E & 0 \\ 0 & 0 \end{bmatrix}, & \overline{\mathbf{C}}_H &= \begin{bmatrix} c_H & 0 \\ 0 & 0 \end{bmatrix}, \\ \overline{\mathbf{G}} &= \begin{bmatrix} 0 & 0 \\ 0 & -I_p \end{bmatrix}, & \overline{\mathbf{K}} &= \begin{bmatrix} k_{22} & k_{23} \\ k_{32} & k_{33} \end{bmatrix}, & \mathbf{v}(t) &= \begin{Bmatrix} r(t) \\ \varphi(t) \end{Bmatrix}, \end{aligned}$$

$$\bar{\mathbf{f}}_{cr}(t) = \frac{1}{2}\sigma(t) \left\{ \begin{array}{l} \Delta k_{22}u_{x0} (1 + e^{2j\omega t}) \\ \Delta k_{44}\varphi_{y0} (1 + e^{2j\omega t}) \end{array} \right\}, \quad \bar{\mathbf{f}}_{umb}(t) = \left\{ \begin{array}{l} me\omega^2 e^{j(\omega t + \phi)} \\ 0 \end{array} \right\}.$$

In the crack force expression, the following term is expressed in a series of multiple harmonics through Equation (11), as

$$\begin{aligned} \frac{1}{2}\sigma(t) (1 + e^{2j\omega t}) &= 0.25 + 0.319e^{j\omega t} + 0.25e^{2j\omega t} + 0.106e^{3j\omega t} \\ &\quad - 0.021e^{5j\omega t} + 0.009e^{7j\omega t} + 0.106e^{-j\omega t} - 0.021e^{-3j\omega t} \quad (16) \\ &\quad + 0.009e^{-5j\omega t} + \dots \end{aligned}$$

Equation (16), in a notational form, is expressed as

$$\frac{1}{2}\sigma(t) (1 + e^{2j\omega t}) = \sum_{i=-n}^{i=n} p_i e^{ji\omega t}. \quad (17)$$

In Equation (17), p_i denotes the coefficient of the i^{th} term in the harmonic function of the crack force excitation, also called the *participation factor* of individual harmonics. The coefficients are small for higher-order harmonics and they do not depend on the crack depth, for the whole range of $t_c/R < 0.5$, where, t_c is the crack depth and R is the radius of the shaft. This is an assumption for the hinge model of the crack [17]. Then, the crack force takes the following form

$$\bar{\mathbf{f}}_{cr}(t) = \left\{ \begin{array}{l} \Delta k_{22}u_{x0} \\ \Delta k_{44}\varphi_{y0} \end{array} \right\} \sum_{i=-n}^{i=n} p_i e^{ji\omega t}. \quad (18)$$

Hence, the solution to Equation (15) will be of the following form

$$\mathbf{v}(t) = \sum_{i=-n}^{i=n} \bar{\mathbf{v}}_i e^{ji\omega t}. \quad (19)$$

Hence, noting above equations, the EOM (i.e., Equation (15)) will be having the following form in the frequency domain

$$\begin{aligned} \left[-(i\omega)^2 \begin{bmatrix} m & 0 \\ 0 & I_d \end{bmatrix} + j(i\omega) \left(\begin{bmatrix} c_E & 0 \\ 0 & 0 \end{bmatrix} + \begin{bmatrix} c_H & 0 \\ 0 & 0 \end{bmatrix} + j\omega \begin{bmatrix} 0 & 0 \\ 0 & I_p \end{bmatrix} \right) \right. \\ \left. + \left(\begin{bmatrix} k_{22} & k_{23} \\ k_{32} & k_{33} \end{bmatrix} - j\omega \begin{bmatrix} c_H & 0 \\ 0 & 0 \end{bmatrix} \right) \right] \bar{\mathbf{v}}_i = \mathbf{f}_i \quad (20) \end{aligned}$$

with

$$\mathbf{f}_i = \left\{ \begin{array}{l} \Delta k_{22}u_{x0} \\ \Delta k_{44}\varphi_{y0} \end{array} \right\} \sum_{i=-n}^{i=n} p_i + \left\{ \begin{array}{l} me\omega^2 e^{j\phi} \\ 0 \end{array} \right\}_{i=1} + j\omega c_H \left\{ \begin{array}{l} u_{x0} \\ 0 \end{array} \right\}_{i=0}.$$

The force term \mathbf{f}_i is represented in the following form

$$\begin{aligned}
 \mathbf{f}_0 &= \begin{Bmatrix} \Delta k_{22}u_{x0} \\ \Delta k_{44}\varphi_{y0} \end{Bmatrix} p_0 + j\omega c_H \begin{Bmatrix} u_{x0} \\ 0 \end{Bmatrix} \quad \text{for } i = 0 \\
 \mathbf{f}_1 &= \begin{Bmatrix} \Delta k_{22}u_{x0} \\ \Delta k_{44}\varphi_{y0} \end{Bmatrix} p_1 + \begin{Bmatrix} me\omega^2 e^{j\phi} \\ 0 \end{Bmatrix} \quad \text{for } i = 1 \\
 \mathbf{f}_i &= \begin{Bmatrix} \Delta k_{22}u_{x0} \\ \Delta k_{44}\varphi_{y0} \end{Bmatrix} \sum_{i=-n}^{i=n} p_i \quad \text{for } i = 2, 3, 5, 7, \dots, -1, -3, -5, \dots
 \end{aligned} \tag{21}$$

The time-domain response of the system, $\mathbf{v}(t)$, is generated through the integration of Equation (15). The forward and backward whirling of the rotor system, $\bar{\mathbf{v}}_i$, can be obtained through the full spectrum of $\mathbf{v}(t)$. The full spectrum extraction from time domain signals and its application are presented in the next section.

3. Generation of full spectrum responses

Equation (19) can be expanded as

$$\begin{aligned}
 \mathbf{v}(t) &= \bar{\mathbf{v}}_0 + \bar{\mathbf{v}}_1 e^{j\omega t} + \bar{\mathbf{v}}_2 e^{2j\omega t} + \bar{\mathbf{v}}_3 e^{3j\omega t} + \bar{\mathbf{v}}_5 e^{5j\omega t} + \dots \\
 &\quad + \bar{\mathbf{v}}_{-1} e^{-j\omega t} + \bar{\mathbf{v}}_{-3} e^{-3j\omega t} + \bar{\mathbf{v}}_{-5} e^{-5j\omega t} + \dots \tag{22}
 \end{aligned}$$

In the above equation, the aim is to obtain various terms, $\bar{\mathbf{v}}_0, \bar{\mathbf{v}}_1, \bar{\mathbf{v}}_{-1}, \bar{\mathbf{v}}_2, \bar{\mathbf{v}}_{-2}, \dots$. It should be noted that these are complex quantities, and it gives amplitude and phase corresponding to various harmonics, $\omega, -\omega, 2\omega, -2\omega, \dots$, which in graphical representation is called the full spectrum. Two procedures are described below to extract the full spectrum.

3.1. Full spectrum based on regression method

For the estimation of unknown complex displacement, i.e., full spectrum displacements, Equation (22) gives the following regression equation (for the present case only up to 7th positive and up to 5th negative harmonic expressions are illustrated)

$$\mathbf{A}_{1_{n \times 9}}(t) \bar{\mathbf{v}}_{i_{9 \times 1}} = \mathbf{v}_{n \times 1}(t). \tag{23}$$

The details of vector matrices $\mathbf{A}_{1_{n \times 9}}(t)$, $\bar{\mathbf{v}}_{i_{9 \times 1}}$ and $\mathbf{v}_{n \times 1}(t)$ are given in Appendix A (Equation (A6)). For the estimation of the unknown vector from Equation (23), time domain displacement responses $\mathbf{v}(t)_{n \times 1}$ will be used as an input that is obtained by time integration discussed earlier (or in the case of the experimental setup, it can

be measured directly). Now, for the computation of unknown vector, Equation (23) may be expressed as

$$\bar{\mathbf{v}}_{i_{9 \times 1}} = \left(\mathbf{A}_1^T \mathbf{A}_1 \right)^{-1} \mathbf{A}_1^T \mathbf{v}(t). \quad (24)$$

The estimates, $\bar{\mathbf{v}}_{i_{9 \times 1}}$, thus found from Equation (24), are in the complex form and they represent complex displacement at various harmonics (both in the forward and backward directions). The above estimation requires large data to be handled in the time domain, which is time consuming, so FFT-based full spectrum has been explained in the next subsection. However, it gives a phase shift, and the correction of it is also explained in the next subsection.

3.2. FFT-based full spectrum estimation

It is known that the FFT is the most popular tool to convert time domain signals to the frequency domain. The FFT is a practical tool as compared to the estimation of full-spectrum based on the regression equation (i.e., Equation (24)) due to its computation efficiency. However, it is seen that during FFT of signals, the amplitudes of various harmonics remain unaffected, but the phases contain an anomaly. To avoid this anomaly, it is required to pass a time domain signal to the FFT algorithm starting at the same time instants with respect to a reference signal. Moreover, to avoid leakage error (which gives anomaly in both amplitude and phase), the signals must have a complete cycle, (i.e., $\omega t = 2\pi n$ with n is an integer). It is very difficult to capture a signal in the aforementioned methods for all practical purposes. An adequate phase compensation can be provided for removing the ambiguity in phase, which is due to random instant picking of the time domain signal, to match the rotor system configuration with the help of a reference signal. In this work, with the help of a reference signal, the phase compensation has been provided.

The full-spectrum estimation methodology is given in the form of a flowchart, as shown in Fig. 4. In which, $|\bar{v}_i(\omega)|$ is the magnitude and $\angle \theta_i$ is the phase of i^{th} harmonic of the response displacement, where i is an integer (positive as well as negative). The multiple harmonic complex reference signal is used for all signal analyses, the harmonics that are mentioned in the flowchart are only required to be present in the reference signal. Conversion of time domain quadrature reference signal to the frequency domain has been carried out using the FFT process. In the flowchart, $|X_i|$ and $\angle \psi_i$ are the magnitude and phase of i^{th} harmonic of the reference signal, respectively. The compensated full spectrum is expressed as [21].

$$\bar{v}_{ci} = |\bar{v}_i(\omega)| \angle (\theta_i - \psi_i), \quad (25)$$

where $\bar{v}_{ci} = R_{i_{re}} + jR_{i_{im}}$ is the corrected full-spectrum complex displacement. Initially, the identification of system parameters is performed by both methods described in this section, viz., the regression-based and FFT-based methods, and are compared for the correctness and their accuracy.

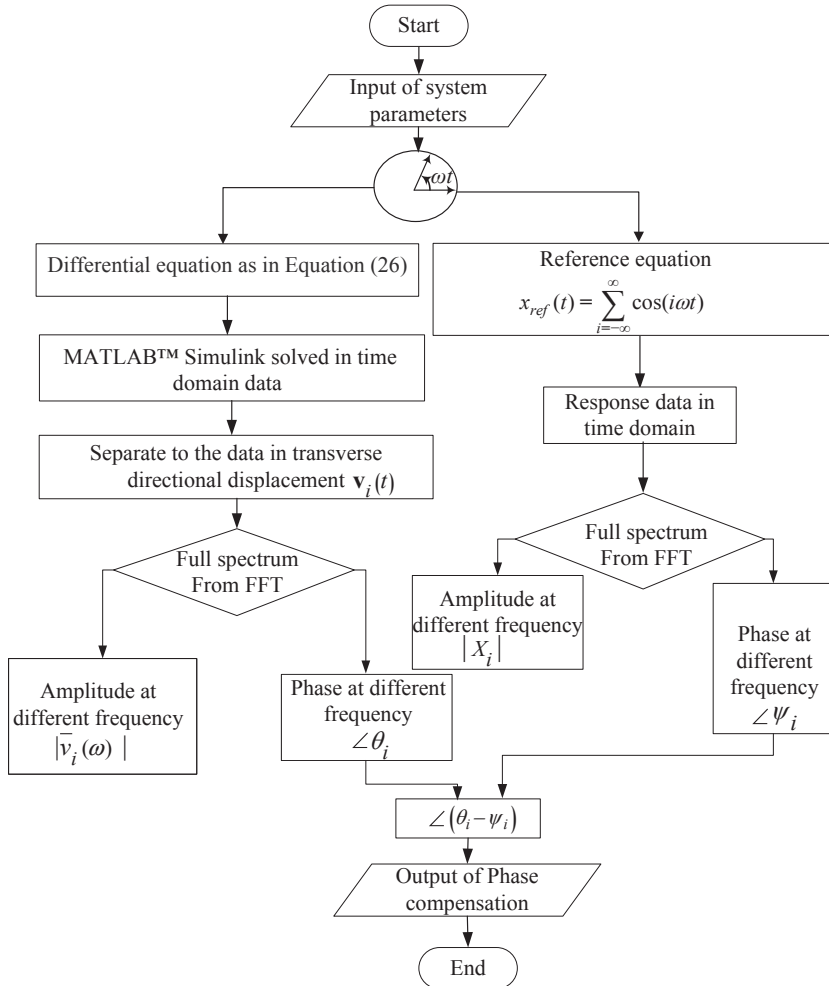


Fig. 4. A flowchart for the full spectrum phase compensation processing

4. Identification of internal damping and other rotor parameters

In this section, an estimation procedure will be developed to estimate the rotor system parameters, like the internal damping, external damping, additive crack stiffness and unbalance, which are not possible to predict by modeling. The developed procedure will use the system responses and some of the system parameters, like the mass of discs and stiffness of the shaft. The procedure will use the EOM Equation (20) to convert it to a regression form for estimation of the parameters. However, it contains the rotational DOFs, the measurement of such responses, in practice, is very difficult. To overcome this practical difficulty, the dynamic reduction scheme has been used in the identification procedure.

4.1. Application of the dynamic reduction scheme

With this scheme, rotational DOFs are eliminated. In Equation (20), the translation and rotational DOFs are considered as the slave and master DOFs, respectively. The master and slave are represented with subscripts m and s , respectively. The crack force in right-hand side of Equation (20) due to rotational DOFs can be neglected in developing the transformation. The partitioned form of the equation takes the following form

$$\begin{aligned} & \left(-(i\omega)^2 \begin{bmatrix} \mathbf{M}_{mm} & 0 \\ 0 & \mathbf{M}_{ss} \end{bmatrix} + j(i\omega) \left(\begin{bmatrix} \mathbf{C}_{mm} & \mathbf{C}_{ms} \\ \mathbf{C}_{sm} & \mathbf{C}_{ss} \end{bmatrix} - j\omega \begin{bmatrix} 0 & 0 \\ 0 & \mathbf{G}_{ss} \end{bmatrix} \right) \right. \\ & \left. + \left(\begin{bmatrix} \mathbf{K}_{mm} & \mathbf{K}_{ms} \\ \mathbf{K}_{sm} & \mathbf{K}_{ss} \end{bmatrix} - j\omega \begin{bmatrix} \mathbf{C}_{H_{mm}} & 0 \\ 0 & 0 \end{bmatrix} \right) \right) \begin{Bmatrix} \mathbf{q}_{mm} \\ \mathbf{q}_{ss} \end{Bmatrix} = \begin{Bmatrix} \mathbf{f}_i \\ \mathbf{0} \end{Bmatrix}. \end{aligned} \quad (26)$$

The details of the matrices mentioned in equation (26) are given in Appendix A (Equation (A7)). The dynamic condensation transformation matrix, \mathbf{T}^D , is obtained as

$$\mathbf{q}_{mm} = \mathbf{I}\mathbf{q}_{mm}; \quad \begin{Bmatrix} \mathbf{q}_{mm} \\ \mathbf{q}_{ss} \end{Bmatrix} = \mathbf{T}^D \mathbf{q}_{mm} \quad (27)$$

with

$$\mathbf{T}^D = \begin{Bmatrix} \mathbf{I} \\ \mathbf{L}_i \end{Bmatrix} \quad \text{where} \quad \mathbf{L}_i = \frac{-\mathbf{K}_{sm}}{\mathbf{K}_{ss} + i\omega^2 \mathbf{G}_{ss} - (i\omega)^2 \mathbf{M}_{ss}}.$$

Here ω is assumed to be the central frequency in the range of frequency of interest. Using this transformation and including the crack force due to rotational DOFs in Equation (26), we get

$$\begin{aligned} & (\mathbf{T}^D)^T \left[-(i\omega)^2 \begin{bmatrix} m & 0 \\ 0 & I_d \end{bmatrix} + ij\omega \begin{bmatrix} c_E & 0 \\ 0 & 0 \end{bmatrix} + (i-1)j\omega \begin{bmatrix} c_H & 0 \\ 0 & 0 \end{bmatrix} + i\omega^2 \begin{bmatrix} 0 & 0 \\ 0 & -I_p \end{bmatrix} \right. \\ & \left. + \begin{bmatrix} k_{22} & k_{23} \\ k_{32} & k_{33} \end{bmatrix} \right] \mathbf{T}^D \mathbf{q}_{mm} = (\mathbf{T}^D)^T \left(\begin{Bmatrix} \Delta k_{22} u_{x0} \\ \Delta k_{44} \varphi_{y0} \end{Bmatrix} \sum_{i=-n}^{i=n} p_i \right. \\ & \left. + \begin{Bmatrix} m e \omega^2 e^{j\varphi} \\ 0 \end{Bmatrix}_{i=1} + j\omega c_H \begin{Bmatrix} u_{x0} \\ 0 \end{Bmatrix}_{i=0} \right). \end{aligned} \quad (28)$$

For typical i^{th} harmonic, \mathbf{T}^D is given as

$$\mathbf{T}_i^D = \begin{bmatrix} 1 & 0 \\ 0 & 1 \\ t_i^d & 0 \\ 0 & t_i^d \end{bmatrix} \quad \text{where} \quad t_i^d = \frac{-k_{42}}{k_{44} - i\omega^2 I_p - (i\omega)^2 I_d}. \quad (29)$$

At the time of development of dynamic condensation transformation, the external force including Δk_{44} in the slave degree of freedom is considered to be zero, and it is again added to the equation after the application of transformation matrix.

In matrix form, the reduced EOM takes the following form

$$\left(-(i\omega)^2 \mathbf{M}^D + ij\omega \mathbf{C}^D + (i-1)j\omega \mathbf{C}_H^D + i\omega^2 \mathbf{G}^D + \mathbf{K}^D \right) \mathbf{q}_{mm} = \mathbf{f}^D. \quad (30)$$

On substituting Equations (A10) through (A15) into Equation (30) and combining together in a complex form with $\mathbf{q}_{mm} = R_i$, we get a single equation, as

$$\begin{aligned} & \left(-(i\omega)^2 m_i + ij\omega(c_E) + (i-1)j\omega c_H - i\omega^2 I_p \left(t_i^d \right)^2 + k_i \right) R_i \\ & = m\omega^2 e^{j\phi} + \left(\Delta k_{22} u_{x0} + t_i^d \Delta k_{44} \varphi_{y0} \right) p_i + j\omega c_H u_{x0} \end{aligned} \quad (31)$$

with $m_i = \left\{ m + \left(t_i^d \right)^2 I_d \right\}$; $k_i = \left\{ k_{22} + 2t_i^d k_{24} + \left(t_i^d \right)^2 k_{44} \right\}$ and $R_i = R_{i\text{Re}} + jR_{i\text{Im}}$.

Real terms of the above equation give

$$\begin{aligned} & -i\omega(c_E) R_{i\text{Im}} - (i-1)\omega c_H R_{i\text{Im}} - m\omega^2 e_{\text{Re}} - \left(\Delta k_{22} u_{x0} + t_i^d \Delta k_{44} \varphi_{y0} \right) p_i \\ & = \left((i\omega)^2 m_i + i\omega^2 I_p \left(t_i^d \right)^2 - k_i \right) R_{i\text{Re}}. \end{aligned} \quad (32)$$

Similarly, imaginary terms give

$$\begin{aligned} & i\omega(c_E) R_{i\text{Re}} + \left((i-1)R_{i\text{Re}} - u_{x0} \right) \omega c_H - m\omega^2 e_{\text{Im}} = \\ & \left((i\omega)^2 m_i + i\omega^2 I_p \left(t_i^d \right)^2 - k_i \right) R_{i\text{Im}}. \end{aligned} \quad (33)$$

Further Equations (32) and (33) are rearranged in the matrix form for the identification of unknown parameters for various harmonics of the switching crack function as

$$\mathbf{A} \mathbf{x} = \mathbf{b}. \quad (34)$$

In the identification, the unknown parameter vector is $\mathbf{x} = \{c_E \ c_H \ e_{\text{Re}} \ e_{\text{Im}} \ \Delta k_{22} \ \Delta k_{44}\}^T$ and the details of other matrices, such as \mathbf{A} and \mathbf{b} , in the above equation (34) are given in Appendix A (Equations (A8) and (A9)). To estimate \mathbf{x} , Equation (34) takes the following form

$$\mathbf{x} = \left(\mathbf{A}^T \mathbf{A} \right)^{-1} \mathbf{A}^T \mathbf{b}. \quad (35)$$

The identification of \mathbf{x} is reliable for multiple speeds of interest. On combining for different spin speeds $\omega_1, \omega_2, \dots, \omega_n$, (with the assumption, parameters to be estimated are speed-independent), Equation (34) may be written as

$$\begin{bmatrix} \mathbf{A}(\omega_1) \\ \mathbf{A}(\omega_2) \\ \vdots \\ \mathbf{A}(\omega_n) \end{bmatrix} \mathbf{x} = \begin{bmatrix} \mathbf{b}(\omega_1) \\ \mathbf{b}(\omega_2) \\ \vdots \\ \mathbf{b}(\omega_n) \end{bmatrix}. \quad (36)$$

Now the analysis and identification procedures developed in foregoing sections are illustrated through numerical simulation.

5. Numerical simulations

A numerical simulation has been done through the Simulink model in MATLABTM environment to obtain the time-domain data from EOMs, as in Equation (15). The Simulink block for the proposed rotor system is shown in Fig. 5. The simulation runs for 8 s duration. Responses have been considered for complete cycles (n) and incomplete cycles (in between $(n-1)$ to n cycle) in the time domain for the same speed of the rotor.

5.1. Time-domain and full-spectrum response

For the numerical simulation, initially, rotor system parameters are assumed, which are summarized in Table 1. The generated responses have been considered for n -complete cycles during 6 to 7 s duration. Initial 6 s response has been removed to avoid transients. Time-domain signals have been generated for the value of ωt , in which, $\omega = 2\pi n$, where n is considered as an integer.

Table 1.

Assumed initial parameter of rotor model for the numerical solution

Parameters		Value	Unit
Mass of disc	m	2	kg
Mass moment of inertia	I_p	0.0048	kg · m ²
	I_d	0.0024	kg · m ²
Intact shaft stiffness	k_{22}	5.779×10^5	N/m
	k_{24}	2.2016×10^4	N
	k_{44}	1.7613×10^4	Nm
Additive crack stiffness	Δk_{22}	1.7337×10^5	N/m
	Δk_{44}	1.7612×10^3	Nm
External damping	c_E	27	Ns/m
Internal damping	c_H	20	Ns/m
Phase of unbalance	ϕ	30	deg
Shaft deflection	u_{x0}	3.57×10^{-5}	m
	φ_{y0}	-4.46×10^{-5}	rad
Disc eccentricity	e	3×10^{-5}	m
Length of shaft	l	0.36	m
	a	0.20	m
	b	0.16	m

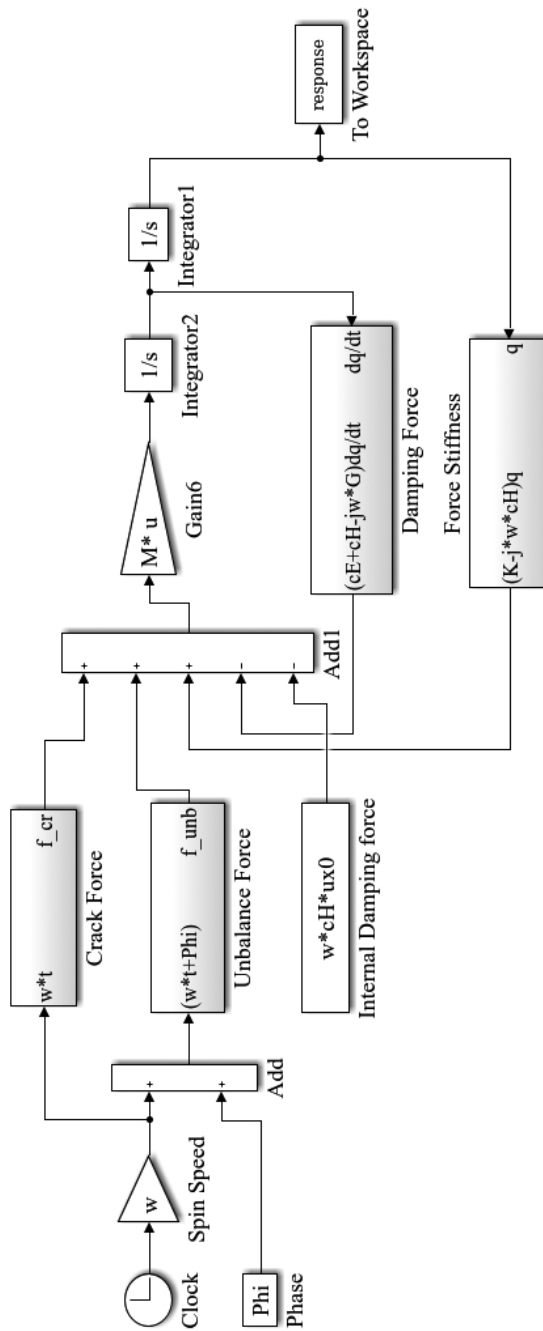


Fig. 5. Simulink block of rotor system

The time domain response generated through Simulink block for 20 Hz is shown in Fig. 6. The plot shows both the vertical and horizontal displacement responses, orbit plots, and a vertical reference signal in Fig. 6a–6d, respectively. Orbit plots show that, as the spin speed has increased, the unbalance force is dominating, and looping due to multi-harmonics of crack forces is insignificant. The fundamental natural frequency (ω_{nf}) of the intact rotor system is 538 rad/s (85.63 Hz).

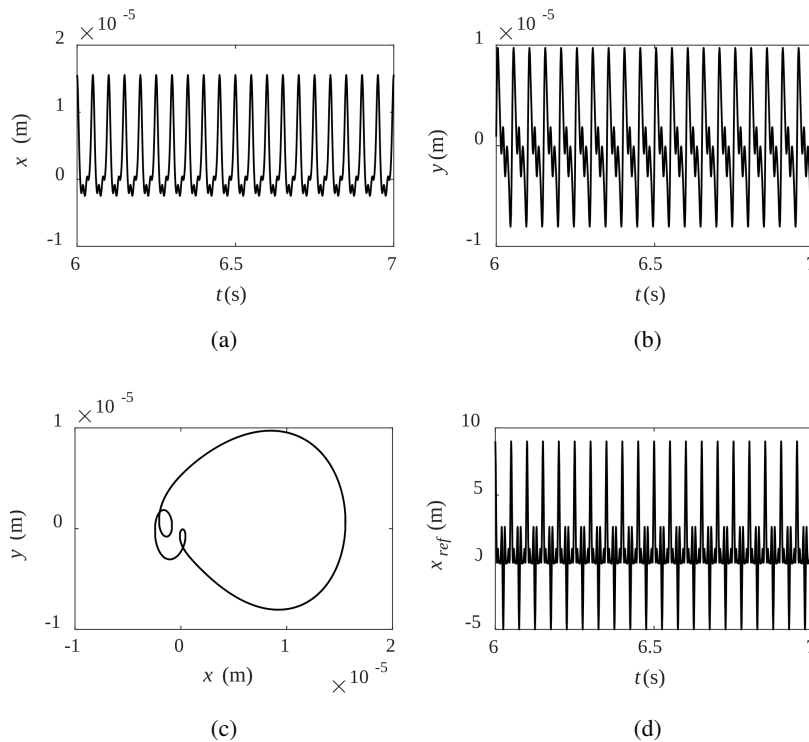


Fig. 6. Time-domain response generated at spin speed of 20 Hz: (a) vertical displacement, x , versus time, (b) horizontal displacement, y , versus time, (c) orbit plot (x versus y) and (d) vertical reference displacement, x_{ref} , versus time

Full-spectrum responses of the proposed rotor system have been generated based on the time-domain responses. Responses of full spectrum show amplitude and phase without and with phase compensation for a spin speed of 20 Hz in Fig. 7. The full-spectrum amplitude for the complete and incomplete cycle of time domain signals using the regression-based full spectrum and FFT-based full spectrum are compared in Table 2 for a spin speed of 20 Hz. The amplitudes of the response for both forward and backward whirling conditions of the rotor are found to be similar for the complete cycle of signals with both the regression and FFT-based full spectrums. However, the amplitudes for the incomplete cycle using the above

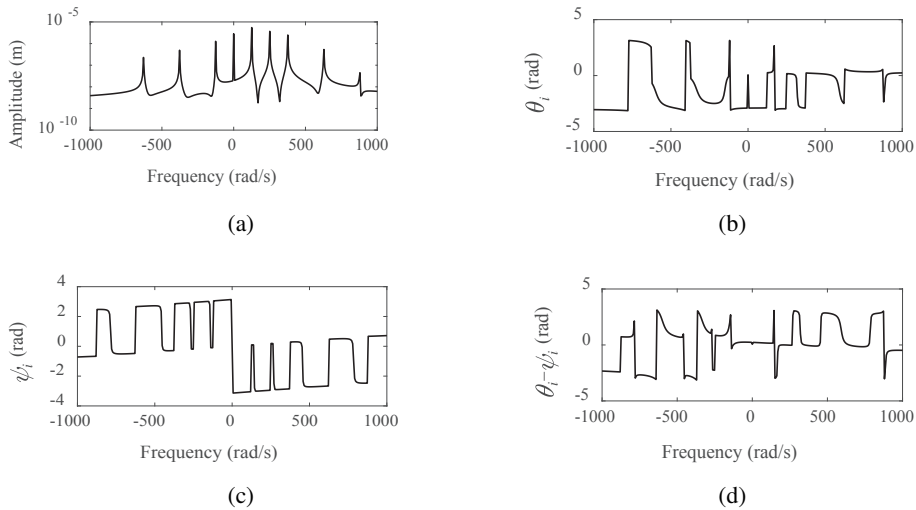


Fig. 7. Full spectrum response at 20 Hz (a) amplitude and (b) phase without compensation, (c) phase of reference signal and (d) phase with compensation

Table 2.

Comparison of full spectrum amplitudes at different harmonics based on the complete and incomplete cycles of displacement signals at 20 Hz

Frequency	Complete cycle		Incomplete cycle	
	Regression based (10^{-6} m)	FFT based (10^{-6} m)	Regression based (10^{-6} m)	FFT based (10^{-6} m)
0	2.8563	2.8563	2.8563	2.8372
ω	5.5201	5.5201	5.5201	5.4937
2ω	3.7056	3.7056	3.7056	3.6788
3ω	2.5063	2.5063	2.5063	2.4855
5ω	0.5434	0.5434	0.5434	0.5339
7ω	0.0562	0.0562	0.0565	0.0448
$-\omega$	1.2824	1.2824	1.2824	1.2711
-3ω	0.4943	0.4943	0.4943	0.4918
-5ω	0.2334	0.2334	0.2334	0.2283

mentioned two methods have some difference. In fact, the full-spectrum amplitudes generated through the regression-based method for complete and incomplete cycles of signals are found to be the same. However, the variation observed in amplitudes by the FFT-based full spectrum for incomplete cycle case differs in only some decimal points with that of the complete cycle.

The comparison of full-spectrum phase for the spin speed of 20 Hz for both complete and incomplete cycles of signals using the regression and FFT-based

Table 3.

Comparison of full spectrum phases (θ_i) at different harmonics based on the complete and incomplete cycles of displacement signals at 20 Hz

Frequency	Complete cycle		Incomplete cycle	
	Regression based (rad)	FFT based (rad)	Regression based (rad)	FFT based (rad)
0	0.0616	0.0616	0.0616	0.0604
ω	0.1597	0.1597	0.5432	0.2557
2ω	-0.0219	-0.0219	0.7450	0.1696
3ω	-0.0572	-0.0572	1.0932	0.2298
5ω	0.1114	0.1114	2.0289	0.5827
7ω	-3.1028	-3.1028	-0.4184	-2.3554
$-\omega$	0.0162	0.0162	-0.3673	-0.0827
-3ω	-3.0657	-3.0657	2.0670	2.9361
-5ω	3.0089	3.0089	1.0914	2.5459

method is provided in Table 3. The values of phase for the complete cycle considering the two methods are found to be similar, and these are correct values. In the case of an incomplete cycle, these values of phase show appreciable variation with respect to correct values using both regression and FFT-based methods. So, in order to remove the variation caused by the leakage error, the complete cycles are collected with the help of a reference signal. In Table 4, the reference signal full-spectrum phase angle is compared both with complete and incomplete

Table 4.

Comparison of full spectrum phases (ψ_i) at different harmonics by the regression and FFT based methods on the complete and incomplete cycles of reference signals at 20 Hz

Frequency	Complete cycle		Incomplete cycle	
	Regression based 10^{-14} (rad)	FFT based 10^{-14} (rad)	Regression based (rad)	FFT based (rad)
0	0.0011	0	0.0006	0
ω	-2.4634	-3.1921	0.3842	0.0960
2ω	-4.8942	-6.3477	0.7686	0.1918
3ω	-21.5703	-28.0384	1.1514	0.2879
5ω	1.9627	2.5495	1.9185	0.4798
7ω	-31.3823	-40.7641	2.6866	0.6714
$-\omega$	2.4303	3.1921	-0.3830	-0.0959
-3ω	21.5779	28.03841	-1.1503	-0.2879
-5ω	-1.9625	-2.5495	-1.9175	-0.4798

cycles of signals using methods mentioned above. The phase values of the reference signal on considering the complete cycle turn out to be zero ($\approx 10^{-14}$) using both methods, which confirms that there is no phase compensation required for a complete cycle. In the case of incomplete cycles of signals, the phase angle shows appreciable deviations, which are found to be dissimilar for both the methods. To perform the phase compensation in the signal due to the FFT-based method also a reference signal is required, as shown in Fig. 4.

The phase compensation for the incomplete cycle is done, and the phase values obtained are found to be similar to those obtained from the complete cycle using both methods, as given in Table 5. From these tables, it is seen that the phase compensation is required if incomplete cycles are considered to avoid leakage errors. Similarly, for different spin speeds, the amplitudes and phases are obtained, and are used in equation (36) for multiple or combined speeds to obtain identification parameters, as summarized in Table 6.

Table 5.

Comparison of phase compensation ($\theta_i - \psi_i$) at different harmonics by the regression and FFT based methods on the complete and incomplete cycles of displacement signals at 20 Hz

Frequency	Complete cycle		Incomplete cycle	
	Regression based (rad)	FFT based (rad)	Regression based (rad)	FFT based (rad)
0	0.0616	0.0616	0.0609	0.0604
ω	0.1597	0.1597	0.1590	0.1597
2ω	-0.0219	-0.0219	-0.0235	-0.0222
3ω	-0.0572	-0.0572	-0.0581	-0.0581
5ω	0.1114	0.1114	0.1104	0.1029
7ω	-3.1028	-3.1028	-3.1050	-3.0268
$-\omega$	0.0162	0.0162	0.0157	0.0133
-3ω	-3.0657	-3.0657	3.2173	-3.0591
-5ω	3.0089	3.0089	3.0089	3.0258

The results obtained using complete cycles of signals are found to be accurate, whereas for incomplete cycles with phase compensation a small variation is obtained between the assumed and identified parameters, except for the crack stiffness due to tilting, Δk_{44} . To check the robustness of the identification algorithm, different percentage of random white noise, i.e., 1%, 2%, and 5% are incorporated in the time domain response of the rotor system, and the results are shown in Fig. 8. The identified parameters, excluding Δk_{44} , shows very small variation ($< 0.15\%$) and ($< 0.7\%$) with consideration of the complete cycle and incomplete cycles with phase compensation, respectively, for the combined speed case. The parameter Δk_{44} shows moderate variation even for the combined speed, i.e., ($< 7\%$) and

Table 6.

Parameters on combined speeds with noise addition

Input speed in Hz	Comparission	Parameters						
		c_H (Nsm ⁻¹)	c_E (Nsm ⁻¹)	e (10 ⁻⁵ m)	ϕ (deg.)	Δk_{22} (10 ⁵ N/m)	Δk_{44} (10 ³ Nm/rad)	
	Assumed value	20	27	3	30	1.7337	1.7613	
	noise	Complete cycle						
Combined speed 20:50 Hz with increment of 1 Hz	A* and B*	add 0% variation	20.0000 (0.000%)	27.0000 (0.000%)	3.0000 (0.000%)	30.0000 (0.000%)	1.7338 (0.006%)	1.7596 (-0.009%)
		add 1% variation	20.0029 (0.014%)	26.9987 (-0.005%)	3.0000 (0.000%)	29.9999 (-0.000%)	1.7334 (-0.017%)	1.7835 (1.260%)
		add 2% variation	20.0058 (0.029%)	26.9974 (-0.009%)	3.0001 (0.003%)	29.9997 (-0.001%)	1.7330 (-0.040%)	1.8074 (2.617%)
		add 5% variation	20.0147 (0.073%)	26.9937 (0.023%)	3.0003 (0.010%)	29.9994 (-0.002%)	1.7319 (-0.104%)	1.8792 (6.694%)
			Incomplete cycle					
	A*	add 0%	19.7199	-22.3227	4.0062	77.03739	12.6407	-713.9713
	B*	add 0% variation	19.8639 (-0.680%)	27.0806 (0.298%)	2.9993 (-0.023%)	29.9329 (-0.223%)	1.7341 (0.023%)	1.7445 (-0.954%)
		add 1% variation	19.8643 (-0.678%)	27.0803 (0.297%)	2.9994 (-0.020%)	29.9329 (-0.223%)	1.7339 (0.011%)	1.7583 (-0.170%)
		add 2% variation	19.8646 (-0.677%)	27.0800 (0.296%)	2.9994 (-0.020%)	29.9329 (-0.223%)	1.7336 (-0.006%)	1.7721 (0.613%)
		add 5% variation	19.8655 (-0.672%)	27.0790 (0.292%)	2.9996 (-0.013%)	29.9328 (-0.224%)	1.7330 (-0.040%)	1.8136 (2.969%)

A* – without phase compensation, **B*** – with phase compensation

(< 3%) for the complete cycle and incomplete cycles with phase compensation, respectively, as shown in Fig. 8.

6. Conclusions

The identification of internal viscous damping due to a combination of rubbing of crack surfaces and hysteretic (shaft material) in a simple rotor with an offset disc has been performed in the present work. In the present numerical simulation, the rotor was run much below the first critical speed, so it is expected that contribution from the shaft material damping would be insignificant because of the rigid behavior of the uncracked shaft portion, but rubbing of crack front is expected due to relatively heavy disc during rotation of the shaft. The estimates of internal viscous damping can give an indication of the presence of a crack in a rotor system. In addition, the estimation of other system parameters, i.e., the viscous external damping, unbalance, and loss of stiffness has also been performed. For the present rotor system, the responses are generated through the SIMULINK model, which

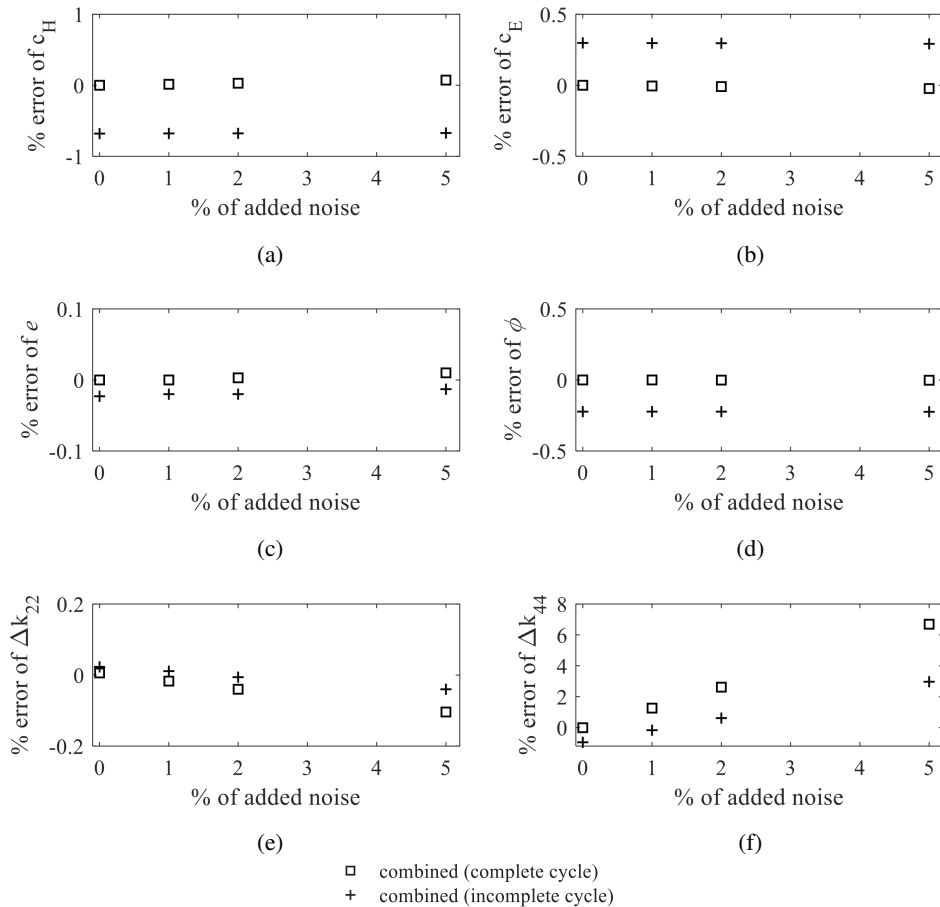


Fig. 8. Percentage error of identification parameters versus percentage addition of noise for (a) internal damping, (b) external damping, (c) eccentricity, (d) phase of unbalance, (e) additive crack stiffness due to transverse force, and (f) additive crack stiffness due to moment

is then transformed to full spectrum through the regression-based and FFT-based methods. In FFT-based method, the phase ambiguity is found and, for the phase compensation, multi-frequency reference signals are used for both complete and incomplete cycle of signal cases. A comparison is made between the estimates, with two full-spectrum generation methods. It is found to be excellent while taking the measurement of the complete cycle and also with phase compensation while taking a measurement of an incomplete cycle. The noise in the measurement test signifies the robustness of the identification algorithm. It is found to be performing well with the responses at combined rotor speeds, except for Δk_{44} , which has slightly higher variation. The present identification algorithm can be extended to a more realistic, the multi-degrees-of-freedom rotor-bearing system, using finite element method.

A. Appendix A: System matrices and vectors

The details of the matrices and vectors mentioned in equation (1) are given as

$$\begin{aligned}
 \mathbf{M} &= \begin{bmatrix} m & 0 & 0 & 0 \\ & m & 0 & 0 \\ & & I_d & 0 \\ \text{sym} & & & I_d \end{bmatrix}; & \mathbf{C}_E &= \begin{bmatrix} c_{22} & 0 & c_{24} & 0 \\ 0 & c_{33} & 0 & c_{35} \\ c_{42} & 0 & c_{44} & 0 \\ 0 & c_{53} & 0 & c_{55} \end{bmatrix}; \\
 \mathbf{K} &= \begin{bmatrix} k_{22} & 0 & k_{24} & 0 \\ & k_{33} & 0 & k_{35} \\ & & k_{44} & 0 \\ \text{sym} & & & k_{55} \end{bmatrix}; & \mathbf{G} &= \begin{bmatrix} 0 & 0 & 0 & 0 \\ 0 & 0 & 0 & 0 \\ 0 & 0 & 0 & I_p \\ 0 & 0 & -I_p & 0 \end{bmatrix}; & (A1) \\
 \mathbf{f}_{umb} &= \begin{Bmatrix} m\omega^2 \cos(\omega t + \phi) \\ m\omega^2 \sin(\omega t + \phi) \\ 0 \\ 0 \end{Bmatrix}; & \mathbf{f}_{st} &= \begin{Bmatrix} mg \\ 0 \\ 0 \\ 0 \end{Bmatrix}; & \mathbf{q} &= \begin{Bmatrix} x \\ y \\ \varphi_y \\ \varphi_x \end{Bmatrix} \\
 \text{and} & \mathbf{q} &= \mathbf{q}_v + \mathbf{q}_0
 \end{aligned}$$

where, m is the mass of disc, I_d is the diametral mass moment of inertia of the disc, I_p is the polar mass moment of inertia of the disc, c_{ij} and k_{ij} represent the external viscous damping and the shaft stiffness in the rotor system, respectively. Subscripts i and j can take values 2, 3, 4 or 5, where 2 and 3 represent shear force direction, and 4 and 5 represent moment directions (refer Fig. 3). 1 and 6 direction represent axial force and torque, respectively; and these effects have been ignored in the present study. Vector \mathbf{q}_0 contains the transverse translatory and angular displacements of the disc due to the gravity force, \mathbf{q}_v contains the transverse translatory and angular displacements of the disc due to dynamic forces on the rotor.

Equation (6) in expanded form takes the following form

$$\mathbf{f}_{cd}(t) = \begin{bmatrix} c_E + c_H & 0 & 0 & 0 \\ 0 & c_E + c_H & 0 & 0 \\ 0 & 0 & 0 & 0 \\ 0 & 0 & 0 & 0 \end{bmatrix} \begin{Bmatrix} \dot{x} \\ \dot{y} \\ \dot{\varphi}_y \\ \dot{\varphi}_x \end{Bmatrix} + \omega \begin{bmatrix} 0 & c_H & 0 & 0 \\ -c_H & 0 & 0 & 0 \\ 0 & 0 & 0 & 0 \\ 0 & 0 & 0 & 0 \end{bmatrix} \begin{Bmatrix} x \\ y \\ \varphi_y \\ \varphi_x \end{Bmatrix}. \quad (A2)$$

Herein, it is assumed that $c_{22} = c_{33} = c_E$ and the value of c_{44} , c_{55} , c_{35} , c_{24} , c_{42} , and c_{53} are taken to be zero.

The details of the matrices mentioned in equation (7) are given as

$$\mathbf{C}_E = \begin{bmatrix} c_E & 0 & 0 & 0 \\ 0 & c_E & 0 & 0 \\ 0 & 0 & 0 & 0 \\ 0 & 0 & 0 & 0 \end{bmatrix}; \quad \mathbf{C}_H = \begin{bmatrix} c_H & 0 & 0 & 0 \\ 0 & c_H & 0 & 0 \\ 0 & 0 & 0 & 0 \\ 0 & 0 & 0 & 0 \end{bmatrix}; \quad \mathbf{C}_{1H} = \begin{bmatrix} 0 & c_H & 0 & 0 \\ -c_H & 0 & 0 & 0 \\ 0 & 0 & 0 & 0 \\ 0 & 0 & 0 & 0 \end{bmatrix}. \quad (A3)$$

Detail of the static deflection $\mathbf{K}\mathbf{q}_0 = \mathbf{f}_{st}$, for Equation (8)

$$\begin{bmatrix} k_{22} & 0 & k_{24} & 0 \\ & k_{33} & 0 & k_{35} \\ & & k_{44} & 0 \\ \text{sym} & & & k_{55} \end{bmatrix} \begin{pmatrix} u_{x0} \\ u_{y0} \\ \varphi_{y0} \\ \varphi_{x0} \end{pmatrix} = \begin{pmatrix} mg \\ 0 \\ 0 \\ 0 \end{pmatrix} \quad (\text{A4})$$

After expanding the above matrix, we get

$$\left. \begin{aligned} u_{x0} &= \frac{mgk_{44}}{k_{44}k_{22} - k_{24}^2} \\ u_{y0} &= 0 \\ \varphi_{y0} &= \frac{mgk_{24}}{k_{24}^2 - k_{44}k_{22}} \\ \varphi_{x0} &= 0 \end{aligned} \right\} \text{ and } \mathbf{q}(t) = \mathbf{q}_v(t) + \mathbf{q}_0$$

$$\text{where, } \mathbf{q}_v(t) = \begin{pmatrix} u_x(t) \\ u_y(t) \\ \varphi_y(t) \\ \varphi_x(t) \end{pmatrix} \quad \text{and} \quad \mathbf{q}_0 = \begin{pmatrix} u_{x0} \\ 0 \\ \varphi_{y0} \\ 0 \end{pmatrix}. \quad (\text{A5})$$

The details of the vector matrices mentioned in equation (23) are given as

$$\mathbf{A}_{1_{n \times 9}}(t) = \begin{bmatrix} 1 & e^{j\omega t_1} & e^{j2\omega t_1} & e^{j3\omega t_1} & e^{j5\omega t_1} & e^{j7\omega t_1} & e^{-j\omega t_1} & e^{-j3\omega t_1} & e^{-j5\omega t_1} \\ 1 & e^{j\omega t_2} & e^{j2\omega t_2} & e^{j3\omega t_2} & e^{j5\omega t_2} & e^{j7\omega t_2} & e^{-j\omega t_2} & e^{-j3\omega t_2} & e^{-j5\omega t_2} \\ 1 & e^{j\omega t_3} & e^{j2\omega t_3} & e^{j3\omega t_3} & e^{j5\omega t_3} & e^{j7\omega t_3} & e^{-j\omega t_3} & e^{-j3\omega t_3} & e^{-j5\omega t_3} \\ \cdot & \cdot \\ \cdot & \cdot \\ 1 & e^{j\omega t_n} & e^{j2\omega t_n} & e^{j3\omega t_n} & e^{j5\omega t_n} & e^{j7\omega t_n} & e^{-j\omega t_n} & e^{-j3\omega t_n} & e^{-j5\omega t_n} \end{bmatrix};$$

$$\bar{\mathbf{v}}_{i_{9 \times 1}} = \begin{pmatrix} \bar{\mathbf{v}}_0 \\ \bar{\mathbf{v}}_1 \\ \bar{\mathbf{v}}_2 \\ \bar{\mathbf{v}}_3 \\ \bar{\mathbf{v}}_5 \\ \bar{\mathbf{v}}_7 \\ \bar{\mathbf{v}}_{-1} \\ \bar{\mathbf{v}}_{-3} \\ \bar{\mathbf{v}}_{-5} \end{pmatrix} \quad \text{and} \quad \mathbf{v}_{n \times 1}(t) = \begin{pmatrix} \mathbf{v}(t_1) \\ \mathbf{v}(t_2) \\ \mathbf{v}(t_3) \\ \vdots \\ \mathbf{v}(t_n) \end{pmatrix}. \quad (\text{A6})$$

The details of the matrices and quantities mentioned in equation (26) are given as

$$\begin{aligned}
 \begin{bmatrix} \mathbf{M}_{mm} & 0 \\ 0 & \mathbf{M}_{ss} \end{bmatrix} &= \begin{bmatrix} m & 0 \\ 0 & I_d \end{bmatrix}; & \begin{bmatrix} \mathbf{C}_{mm} & \mathbf{C}_{ms} \\ \mathbf{C}_{sm} & \mathbf{C}_{ss} \end{bmatrix} &= \begin{bmatrix} c_E & 0 \\ 0 & 0 \end{bmatrix}; \\
 \begin{bmatrix} 0 & 0 \\ 0 & \mathbf{G}_{ss} \end{bmatrix} &= \begin{bmatrix} 0 & 0 \\ 0 & -I_p \end{bmatrix}; & \begin{bmatrix} \mathbf{K}_{mm} & \mathbf{K}_{ms} \\ \mathbf{K}_{sm} & \mathbf{K}_{ss} \end{bmatrix} &= \begin{bmatrix} k_{22} & k_{23} \\ k_{32} & k_{33} \end{bmatrix}; \\
 \begin{bmatrix} \mathbf{C}_{H_{mm}} & 0 \\ 0 & 0 \end{bmatrix} &= \begin{bmatrix} c_H & 0 \\ 0 & 0 \end{bmatrix}; & \left\{ \begin{matrix} \mathbf{q}_{mm} \\ \mathbf{q}_{ss} \end{matrix} \right\} &= \left\{ \begin{matrix} R_i \\ \phi_i \end{matrix} \right\} \quad \text{and} & \quad (A7) \\
 \left\{ \begin{matrix} \mathbf{f}_i \\ \mathbf{0} \end{matrix} \right\} &= \left\{ \begin{matrix} \Delta k_{22} u_{x0} \sum_{i=-n}^{i=n} p_i \\ 0 \end{matrix} \right\} + \left\{ \begin{matrix} m e \omega^2 e^{j\varphi} \\ 0 \end{matrix} \right\}_{i=1} + \left\{ \begin{matrix} \omega c_H u_{x0} e^{j\frac{\pi}{2}} \\ 0 \end{matrix} \right\}_{i=0}
 \end{aligned}$$

The details of the remaining matrices and quantities mentioned in equation (34) are given as

$$\mathbf{A} = \begin{bmatrix} 0 & \omega R_{0\text{Im}} & 0 & 0 & -u_{x0} p_0 & -t_0^d \varphi_{y0} p_0 \\ -\omega R_{1\text{Im}} & 0 & -m\omega^2 & 0 & -u_{x0} p_1 & -t_1^d \varphi_{y0} p_1 \\ -2\omega R_{2\text{Im}} & -\omega R_{1\text{Im}} & 0 & 0 & -u_{x0} p_2 & -t_2^d \varphi_{y0} p_2 \\ -3\omega R_{3\text{Im}} & -2\omega R_{3\text{Im}} & 0 & 0 & -u_{x0} p_3 & -t_3^d \varphi_{y0} p_3 \\ -5\omega R_{5\text{Im}} & -4\omega R_{5\text{Im}} & 0 & 0 & -u_{x0} p_5 & -t_5^d \varphi_{y0} p_5 \\ -7\omega R_{7\text{Im}} & -6\omega R_{7\text{Im}} & 0 & 0 & -u_{x0} p_7 & -t_7^d \varphi_{y0} p_7 \\ \omega R_{-1\text{Im}} & 2\omega R_{-1\text{Im}} & 0 & 0 & -u_{x0} p_{-1} & -t_{-1}^d \varphi_{y0} p_{-1} \\ 3\omega R_{-3\text{Im}} & 4\omega R_{-3\text{Im}} & 0 & 0 & -u_{x0} p_{-3} & -t_{-3}^d \varphi_{y0} p_{-3} \\ 5\omega R_{-5\text{Im}} & 6\omega R_{-5\text{Im}} & 0 & 0 & -u_{x0} p_{-5} & -t_{-5}^d \varphi_{y0} p_{-5} \\ 0 & -\omega (R_{0\text{Re}} + u_{x0}) & 0 & 0 & 0 & 0 \\ \omega R_{1\text{Re}} & 0 & 0 & -m\omega^2 & 0 & 0 \\ 2\omega R_{2\text{Re}} & \omega R_{2\text{Re}} & 0 & 0 & 0 & 0 \\ 3\omega R_{3\text{Re}} & 2\omega R_{3\text{Re}} & 0 & 0 & 0 & 0 \\ 5\omega R_{5\text{Re}} & 4\omega R_{5\text{Re}} & 0 & 0 & 0 & 0 \\ 7\omega R_{7\text{Re}} & 6\omega R_{7\text{Re}} & 0 & 0 & 0 & 0 \\ -\omega R_{-1\text{Re}} & -2\omega R_{-1\text{Re}} & 0 & 0 & 0 & 0 \\ -3\omega R_{-3\text{Re}} & -4\omega R_{-3\text{Re}} & 0 & 0 & 0 & 0 \\ -5\omega R_{-5\text{Re}} & -6\omega R_{-5\text{Re}} & 0 & 0 & 0 & 0 \end{bmatrix} \quad (A8)$$

and

$$\mathbf{b} = \left\{ \begin{array}{l} -k_0 R_{0\text{Re}} \\ \left(\omega^2 m_1 + \omega^2 I_p (t_1^d)^2 - k_1 \right) R_{1\text{Re}} \\ \left(4\omega^2 m_2 + 2\omega^2 I_p (t_2^d)^2 - k_2 \right) R_{2\text{Re}} \\ \left(9\omega^2 m_3 + 3\omega^2 I_p (t_3^d)^2 - k_3 \right) R_{3\text{Re}} \\ \left(25\omega^2 m_5 + 5\omega^2 I_p (t_5^d)^2 - k_5 \right) R_{5\text{Re}} \\ \left(49\omega^2 m_7 + 7\omega^2 I_p (t_7^d)^2 - k_7 \right) R_{7\text{Re}} \\ \left(\omega^2 m_{-1} - \omega^2 I_p (t_{-1}^d)^2 - k_{-1} \right) R_{-1\text{Re}} \\ \left(9\omega^2 m_{-3} - 3\omega^2 I_p (t_{-3}^d)^2 - k_{-3} \right) R_{-3\text{Re}} \\ \left(25\omega^2 m_{-5} - 5\omega^2 I_p (t_{-5}^d)^2 - k_{-5} \right) R_{-5\text{Re}} \\ -k_0 R_{0\text{Im}} \\ \left(\omega^2 m_1 + \omega^2 I_p (t_1^d)^2 - k_1 \right) R_{1\text{Im}} \\ \left(4\omega^2 m_2 + 2\omega^2 I_p (t_2^d)^2 - k_2 \right) R_{2\text{Im}} \\ \left(9\omega^2 m_3 + 3\omega^2 I_p (t_3^d)^2 - k_3 \right) R_{3\text{Im}} \\ \left(25\omega^2 m_5 + 5\omega^2 I_p (t_5^d)^2 - k_5 \right) R_{5\text{Im}} \\ \left(49\omega^2 m_7 + 7\omega^2 I_p (t_7^d)^2 - k_7 \right) R_{7\text{Im}} \\ \left(\omega^2 m_{-1} - \omega^2 I_p (t_{-1}^d)^2 - k_{-1} \right) R_{-1\text{Im}} \\ \left(9\omega^2 m_{-3} - 3\omega^2 I_p (t_{-3}^d)^2 - k_{-3} \right) R_{-3\text{Im}} \\ \left(25\omega^2 m_{-5} - 5\omega^2 I_p (t_{-5}^d)^2 - k_{-5} \right) R_{-5\text{Im}} \end{array} \right\}. \quad (\text{A9})$$

Reduction matrices with exclusion of the slave DOFs for Equation (30) according Equation (29) are given as

$$\mathbf{M}^D = (\mathbf{T}^D)^T \begin{bmatrix} \mathbf{M}_{mm} & \mathbf{0} \\ \mathbf{0} & \mathbf{M}_{ss} \end{bmatrix} \mathbf{T}^D = \begin{bmatrix} m + (t_i^d)^2 I_d & 0 \\ 0 & m + (t_i^d)^2 I_d \end{bmatrix}; \quad (\text{A10})$$

$$\begin{aligned}
 \mathbf{K}^D &= (\mathbf{T}_i^D)^T \begin{bmatrix} \mathbf{K}_{mm} & \mathbf{K}_{ms} \\ \mathbf{K}_{sm} & \mathbf{K}_{ss} \end{bmatrix} \mathbf{T}_i^D \\
 &= \begin{bmatrix} k_{22} + 2t_i^d k_{24} + (t_i^d)^2 k_{44} & 0 \\ 0 & k_{22} + 2t_i^d k_{24} + (t_i^d)^2 k_{44} \end{bmatrix}; \quad (\text{A11})
 \end{aligned}$$

$$\mathbf{C}^D = (\mathbf{T}_i^D)^T \begin{bmatrix} \mathbf{C}_{mm} & \mathbf{C}_{ms} \\ \mathbf{C}_{sm} & \mathbf{C}_{ss} \end{bmatrix} \mathbf{T}_i^D = \begin{bmatrix} c_E & 0 \\ 0 & c_E \end{bmatrix}; \quad (\text{A12})$$

$$\mathbf{C}_H^D = (\mathbf{T}_i^D)^T \begin{bmatrix} \mathbf{C}_{Hmm} & 0 \\ 0 & 0 \end{bmatrix} \mathbf{T}_i^D = \begin{bmatrix} c_H & 0 \\ 0 & c_H \end{bmatrix}; \quad (\text{A13})$$

$$\mathbf{G}^D = (\mathbf{T}_i^D)^T \begin{bmatrix} \mathbf{0} & \mathbf{0} \\ \mathbf{0} & \mathbf{G}_{ss} \end{bmatrix} \mathbf{T}_i^D = \begin{bmatrix} -I_p (t_i^d)^2 & 0 \\ 0 & -I_p (t_i^d)^2 \end{bmatrix}; \quad (\text{A14})$$

$$\mathbf{f}^D = (\mathbf{T}_i^D)^T \begin{Bmatrix} \mathbf{f}_m \\ \mathbf{f}_s \end{Bmatrix} = \begin{Bmatrix} m\omega^2 \cos(\phi) \\ m\omega^2 \sin(\phi) \end{Bmatrix} + \begin{Bmatrix} (\Delta k_{22} u_{x0} + t_i^d \Delta k_{44} \varphi_{y0}) p_i \\ 0 \end{Bmatrix} - \omega \begin{Bmatrix} 0 \\ -c_H u_{x0} \end{Bmatrix}. \quad (\text{A15})$$

Manuscript received by Editorial Board, August 03, 2018;
 final version, March 25, 2019.

References

- [1] R. Tiwari. *Rotor Systems: Analysis and Identification*. CRC Press, Boca Raton, FL, USA, 2017.
- [2] F. Ehrlich. Shaft whirl induced by rotor internal damping. *Journal of Applied Mechanics*, 31(2):279–282, 1964. doi: [10.1115/1.3629598](https://doi.org/10.1115/1.3629598).
- [3] J. Shaw and S. Shaw. Instabilities and bifurcations in a rotating shaft. *Journal of Sound and Vibration*, 132(2):227–244, 1989. doi: [10.1016/0022-460X\(89\)90594-4](https://doi.org/10.1016/0022-460X(89)90594-4).
- [4] W. Kurnik. Stability and bifurcation analysis of a nonlinear transversally loaded rotating shaft. *Nonlinear Dynamics*, 5(1):39–52, 1994. doi: [10.1007/BF00045079](https://doi.org/10.1007/BF00045079).
- [5] L.-W. Chen and D.-M. Ku. Analysis of whirl speeds of rotor-bearing systems with internal damping by C^0 finite elements. *Finite Elements in Analysis and Design*, 9(2):169–176, 1991. doi: [10.1016/0168-874X\(91\)90059-8](https://doi.org/10.1016/0168-874X(91)90059-8).
- [6] D.-M. Ku. Finite element analysis of whirl speeds for rotor-bearing systems with internal damping. *Mechanical Systems and Signal Processing*, 12(5):599–610, 1998. doi: [10.1006/mssp.1998.0159](https://doi.org/10.1006/mssp.1998.0159).
- [7] J. Melanson and J. Zu. Free vibration and stability analysis of internally damped rotating shafts with general boundary conditions. *Journal of Vibration and Acoustics*, 120(3):776–783, 1998. doi: [10.1115/1.2893897](https://doi.org/10.1115/1.2893897).
- [8] G. Genta. On a persistent misunderstanding of the role of hysteretic damping in rotordynamics. *Journal of Vibration and Acoustics*, 126(3):459–461, 2004. doi: [10.1115/1.1759694](https://doi.org/10.1115/1.1759694).
- [9] M. Dimentberg. Vibration of a rotating shaft with randomly varying internal damping. *Journal of Sound and Vibration*, 285(3):759–765, 2005. doi: [10.1016/j.jsv.2004.11.025](https://doi.org/10.1016/j.jsv.2004.11.025).
- [10] F. Vatta and A. Vigliani. Internal damping in rotating shafts. *Mechanism and Machine Theory*, 43(11):1376–1384, 2008. doi: [10.1016/j.mechmachtheory.2007.12.009](https://doi.org/10.1016/j.mechmachtheory.2007.12.009).
- [11] J. Fischer and J. Strackeljan. Stability analysis of high speed lab centrifuges considering internal damping in rotor-shaft joints. *Technische Mechanik*, 26(2):131–147, 2006.

- [12] O. Montagnier and C. Hochard. Dynamic instability of supercritical driveshafts mounted on dissipative supports – effects of viscous and hysteretic internal damping. *Journal of Sound and Vibration*, 305(3):378–400, 2007. doi: [10.1016/j.jsv.2007.03.061](https://doi.org/10.1016/j.jsv.2007.03.061).
- [13] M. Chouksey, J.K. Dutt, and S.V. Modak. Modal analysis of rotor-shaft system under the influence of rotor-shaft material damping and fluid film forces. *Mechanism and Machine Theory*, 48:81–93, 2012. doi: [10.1016/j.mechmachtheory.2011.09.001](https://doi.org/10.1016/j.mechmachtheory.2011.09.001).
- [14] P. Goldman and A. Muszynska. Application of full spectrum to rotating machinery diagnostics. *Orbit*, 20(1):17–21, 1991.
- [15] R. Tiwari. Conditioning of regression matrices for simultaneous estimation of the residual unbalance and bearing dynamic parameters. *Mechanical Systems and Signal Processing*, 19(5):1082–1095, 2005. doi: [10.1016/j.ymsp.2004.09.005](https://doi.org/10.1016/j.ymsp.2004.09.005).
- [16] I. Mayes and W. Davies. Analysis of the response of a multi-rotor-bearing system containing a transverse crack in a rotor. *Journal of Vibration, Acoustics, Stress, and Reliability in Design*, 106(1):139–145, 1984. doi: [10.1115/1.3269142](https://doi.org/10.1115/1.3269142).
- [17] R. Gasch. Dynamic behaviour of the Laval rotor with a transverse crack. *Mechanical Systems and Signal Processing*, 22(4):790–804, 2008. doi: [10.1016/j.ymsp.2007.11.023](https://doi.org/10.1016/j.ymsp.2007.11.023).
- [18] M. Karthikeyan, R. Tiwari, S. and Talukdar. Development of a technique to locate and quantify a crack in a beam based on modal parameters. *Journal of Vibration and Acoustics*, 129(3):390–395, 2007. doi: [10.1115/1.2424981](https://doi.org/10.1115/1.2424981).
- [19] S.K. Singh and R. Tiwari. Identification of a multi-crack in a shaft system using transverse frequency response functions. *Mechanism and Machine Theory*, 45(12):1813–1827, 2010. doi: [10.1016/j.mechmachtheory.2010.08.007](https://doi.org/10.1016/j.mechmachtheory.2010.08.007).
- [20] C. Shrivankumar and R. Tiwari. Identification of stiffness and periodic excitation forces of a transverse switching crack in a Laval rotor. *Fatigue & Fracture of Engineering Materials & Structures*, 36(3):254–269, 2013. doi: [10.1111/j.1460-2695.2012.01718.x](https://doi.org/10.1111/j.1460-2695.2012.01718.x).
- [21] S. Singh and R. Tiwari. Model-based fatigue crack identification in rotors integrated with active magnetic bearings. *Journal of Vibration and Control*, 23(6):980–1000, 2017. doi: [10.1177/1077546315587146](https://doi.org/10.1177/1077546315587146).
- [22] S. Singh and R. Tiwari. Model-based switching-crack identification in a Jeffcott rotor with an offset disk integrated with an active magnetic bearing. *Journal of Dynamic Systems, Measurement, and Control*, 138(3):031006, 2016. doi: [10.1115/1.4032292](https://doi.org/10.1115/1.4032292).
- [23] S. Singh and R. Tiwari. Model based identification of crack and bearing dynamic parameters in flexible rotor systems supported with an auxiliary active magnetic bearing. *Mechanism and Machine Theory*, 122: 292–307, 2018. doi: [10.1016/j.mechmachtheory.2018.01.006](https://doi.org/10.1016/j.mechmachtheory.2018.01.006).
- [24] C. Shrivankumar. Crack Identific in Rotors with Full-Spectrum. Ph.D. Thesis, IIT Guwahati, India, 2014.
- [25] A.D. Dimarogonas. Vibration of cracked structures: a state of the art review. *Engineering Fracture Mechanics*, 55(5): 831–857, 1996. doi: [10.1016/0013-7944\(94\)00175-8](https://doi.org/10.1016/0013-7944(94)00175-8).